Insight into the role of $TiCl_4$ post-treated mesoporous TiO_2 electron transport layer on photovoltaic performance of perovskite solar cells

Amalraj Peter Amalathas*[a], Lucie Landová [ab], Teodor Huminiuc[c], Lukáš Horák[d], Brianna Conrad [a], Tomas Polcar[ce], Jakub Holovský [ab]

[a]Centre for Advanced Photovoltaics, Faculty of Electrical Engineering, Czech Technical University in Prague, Technická 2, 166 27 Prague, Czech Republic

[b]Institute of Physics, Czech Academy of Sciences, v. v. i., Cukrovarnická 10, 162 00 Prague, Czech Republic

[c]Engineering Materials, Faculty of Engineering and Physical Sciences, University of Southampton, Southampton SO17 1BJ, United Kingdom

[d]Department of Condensed Matter Physics, Faculty of Mathematics and Physics, Charles University, Ke Karlovu 5, 12116, Prague 2, Czech Republic

[e]Department of Control Engineering, Faculty of Electrical Engineering, Czech Technical University in Prague, Technická 2, 166 27 Prague, Czech Republic

* Corresponding author: peterama@fel.cvut.cz

Abstract

The ideal electron transport layer of a high performance perovskite solar cell should have a good percolation while being mesoporous, good optical transparency, high electrical conductivity, and an energy level alignment well-matched with the perovskite material. In this work, we investigate the role of $TiCl_4$ post-treatment of the mesoporous TiO_2 electron transport layer by varying the concentration of $TiCl_4$ and characterizing optical and electrical properties, charge carrier dynamics, and particularly the film morphology with the special focus on percolation. We correlate our results with the photovoltaic performance of mesoscopic $CH_3NH_3PbI_3$ solar cells. It is found that the $TiCl_4$ treatment leads to an additional interconnection between the TiO_2 particles, as evident from high resolution cross-section images and chemical maps, improvement of interfacial contact due to a smoother surface, and a significant reduction in sub-bandgap absorption with a lower level of electronic disorder determined by photothermal deflection spectroscopy, leading to higher effective electron mobility in mesoporous TiO_2. This contributes to more efficient charge extraction and suppressed charge recombination in solar cells, resulting in improved V_{OC}, $J_{SC,}$ and FF. Moreover, reduced charge accumulation at the interface results in reduced hysteresis. As a result, the optimized device based on $TiCl_4$ post-treated mesoporous TiO_2 achieved the highest conversion efficiency of 17.4 % compared with 14.1 % for the device with pristine mesoporous TiO_2.

Introduction

Organic-inorganic lead halide perovskite solar cells (PSCs) have drawn rapid widespread attention in the field of photovoltaics due to their high power-conversion efficiency (PCE), along with low cost and facile fabrication process. Moreover, the remarkable structural and optoelectronic properties of perovskite materials, high absorption coefficient with low Urbach energy, long carrier diffusion length, tunable bandgap, high carrier mobility, and photon recycling ability, are regarded as the main reason for the impressive improvement of PSC efficiency[1-6]. The efficiency of PSCs has rapidly increased from 3.8% in 2009 to a recently certified record efficiency of 25.2% in a decade of development via material composition optimization, control of the crystal growth of the film, and interface and device engineering [7-10].

The main components of a typical mesoscopic n-i-p PSC structure are a transparent conductive electrode, an electron transport layer(ETL) including a compact layer and a mesoporous layer, a perovskite active layer, a hole transport layer(HTL) and a back contact metal electrode. In such a device structure, the ETL plays an important role in extracting the electrons from the perovskite layer and transporting them to the conductive electrode and simultaneously assists as a hole blocking layer [11-13]. To date, several n-type metal oxides, such as TiO_2 [14-15], ZnO [16-17], SnO_2 [18-19], Nb_2O_5[20], $SrTiO_3$[21], $ZnTiO_3$[22], Zn_2SnO_4[23], WO_3[24], In_2O_3[25], $BaSnO_3$[26] and CeO_X[27], have been investigated as ETLs in PSCs. Among these, TiO_2 based mesoporous layers have generally been most successful in producing high efficiency in PSCs[28-31]. Although pristine TiO_2 possess the advantages of good chemical stability, high transparency, a well-matched energy level, non-toxicity and low cost, it always suffers from intrinsic drawbacks such as low electron mobility and

conductivity as well as poor film quality with numerous trap states, leading to significant charge accumulation and recombination loss [32-33].

To address this issue, various approaches have been investigated to improve the properties of TiO_2 for efficient carrier extraction and collection using fullerene derivatives[34], amino acids [35], metals[15, 36], graphene[37], thiols[38], carboxyl groups[39] and $TiCl_4$ [40]. Among the various approaches investigated for modifying the surface of TiO_2 film, $TiCl_4$ post-treatment is one of the methods most commonly used in the development of dye-sensitized solar cells to reduce the rate of recombination and improve the charge injection efficiency [41-42]. Similar $TiCl_4$ post-treatment methods have been investigated by some researchers in PSCs to improve the device performance[43-46]. For instance, Liu et al. reported that a uniform and pinhole-free compact TiO_2 layer was obtained using $TiCl_4$ post-treatment, leading to enhanced contact at the TiO_2/perovskite interface, increased charge mobility and suppressed charge recombination[44]. However, in terms of mesoporous TiO_2 layer, a comprehensive understanding of the role of $TiCl_4$ post-treatment with varied conditions is still needed.

In this work, we therefore explore different concentrations of $TiCl_4$ post-treatment applied to mesoporous TiO_2 film and look for changes in morphology, optical properties, level of electronic disorder and charge extraction. We use scanning electron microscope (SEM), transmission electron microscopy (TEM), X-ray diffraction (XRD), photothermal deflection absorption spectroscopy (PDS), space charge limited current technique, steady-state photoluminescence and time-resolved photoluminescence. We further extend the study by correlating our findings with the photovoltaic performance of fabricated perovskite solar cells.

Materials and Methods

Materials

Lead iodide (PbI_2) was purchased from TCI Chemicals. Titanium diisopropoxide bis(acetylacetonate) (75 wt. % in isopropanol), titanium(IV) chloride ($TiCl_4$), lithium bis(trifluoromethanesulfonyl)imide (Li-TFSI), N,N-Dimethylformamide (DMF), dimethyl sulphoxide (DMSO), 4-tert-butyl pyridine and anhydrous ethanol were purchased from Sigma-Aldrich. Titanium dioxide paste (30 NR-D) was purchased from Greatcellsolar and 2,2',7,7'-tetrakis-(N,N-di-4-methoxyphenylamino)-9,9'-spirobifluorene (Spiro- MeOTAD) was purchased from Lumtec. Methylammonium iodide (CH_3NH_3I) and pre-patterned fluorine-doped tin oxide (FTO) coated glass substrates (10 ohms/sq) were purchased from Solaronix. All the chemicals were used as received without further purification.

Fabrication of Perovskite Solar Cells

The glass/FTO substrates were cleaned by sonicating in a 2% solution of Hellmanex detergent diluted in deionized (DI) water for 30 min. After rinsing with DI water, the substrates were further cleaned with acetone and then ethanol in an ultrasonic bath for 15 min each, and dried with nitrogen. A 30 nm compact TiO_2 layer was deposited on the FTO substrates by spray pyrolysis using a precursor solution of titanium diisopropoxide bis(acetylacetonate) (75 wt. % in isopropanol,) in anhydrous ethanol (1/9, V/V) at 450 °C, with O_2 as the carrying gas. Then the substrates were sintered at 500 °C for 30 min and left to cool down slowly to room temperature. A 150 nm mesoporous TiO_2 layer was deposited by spin coating a diluted 30 nm TiO_2 particle paste (30 NR-D) in anhydrous ethanol (150 mg/mL) at 4000 rpm for 20 s with a ramp of 2000 rpm/s. After spin coating, the substrates were immediately dried on a hot plate at 100 °C for 10 min and

then sintered at 500 °C for 60 min. After cooling down to room temperature, the coated mesoporous TiO_2 substrates were immersed in aqueous $TiCl_4$ solutions of different concentrations (20, 40, 80 and 100 mM) at 70 °C for 30 min, then rinsed with DI water and dried with nitrogen. The substrates were again sintered at 450 °C for 30 min on a hot plate under dry airflow and then left to cool down to 150 °C. Then the substrates were immediately moved to a nitrogen-filled glovebox for the deposition of the perovskite films. The perovskite layer was deposited by a two-step spin coating method. 1M PbI_2 solution in anhydrous DMF/ DMSO (9.5/0.5, v/v) was prepared under constant stirring at 70 °C overnight. The PbI_2 solution was first spin-coated on the substrate at 1000 rpm for 40 s, followed by heating at 70 °C for 10 min. Second, after the PbI_2 cooled down, 0.22M CH_3NH_3I dissolved in 2-propanol was spin-coated on top of the PbI_2 layer using a two-step protocol with 60 s of loading time followed by 40 s of spinning at 4000 rpm. After the spin-coating, substrates were annealed at 100 °C for 30 min.

After substrates cooled to room temperature, 50 µl of the hole transporting material Spiro-MeOTAD solution was deposited on top of the perovskite layer by spin coating at 4000 rpm for 30 s. The Spiro-MeOTAD solution was prepared by Spiro- MeOTAD in chlorobenzene (72.3 mg/mL) with the addition of 28.8 µL of 4-tert-butyl pyridine and 17.5 µL of Li-TFSI solution (520 mg Li-TSFI in 1 mL acetonitrile). After storing the devices overnight in a dry box, an 80 nm Au top electrode was deposited by thermal evaporation under high vacuum using a shadow mask to pattern the electrodes.

Device and Material Characterization

The surface morphology of samples was probed using a Tescan MAIA3 SEM, equipped with an ultra-high-resolution regime in high vacuum. XRD measurements were performed using a Rigaku SmartLab diffractometer equipped with a 9 kW copper rotating anode X-ray source (CuKα radiationλ= 0.15418 nm). Absorptance measurements were performed by Photo-thermal deflection spectroscopy (PDS) with a monochromator-based spectrometer with a 150 W xenon lamp. For these measurements, the samples were immersed in Fluorinert liquid FC- 72 with a strongly temperature-dependent refractive index (1.25 at room temperature). Steady-state photoluminescence (PL) measurements were carried out using a Cary Eclipse fluorescence spectrophotometer under excitation at 300 nm. Time-resolved PL (TRPL) measurements were performed via a time-correlated single-photon counting (TCSPC) setup (FluoTime 200, PicoQuant GmbH) excited by a 442 nm (5 MHz) picosecond pulsed laser (LDH-P-C-440B). The current-voltage characteristics of the electron-only devices (FTO/TiO_2/Au) were measured by Keithley 2400 Source in dark conditions. The external quantum efficiency (EQE) measurements were recorded using Bentham unit equipped with a TMC 300 monochromator, 50 W tungsten halogen lamp, and a lock-in amplifier. A calibrated Si photodetector was used as the reference cell. The current density-voltage characteristics (J-V) of the solar cells were obtained using a Keithley 2400 source meter and a solar simulator (Wavelabs) with AM 1.5G filter under the illumination of 100 $mWcm^{-2}$. The light intensity was determined using a calibrated silicon photodiode. The solar cells were masked with a metal mask (0.09 cm^2) to define the active area. All measurements of the devices were carried out under an ambient atmosphere at room temperature without encapsulation.

Results and Discussion

Figure 1 shows the top view SEM images of mesoporous TiO_2 films treated with different $TiCl_4$ concentrations (0,20, 40, 80 and 100 mM) to elucidate the effect of treatment on layer morphology (see Figure S1 for lower magnification SEM images). It is evident that pristine (untreated) mesoporous TiO_2 features small particles with poor percolation and wide distribution of pore sizes and that the particles grow and the small pores were gradually filled when the mesoporous TiO_2 films were treated with $TiCl_4$ resulting in better percolation. The improvement is observed continuously up to 80mM concentrations followed by a growth of non-conformal overlayer of TiO_2 on the top of the mesoporous TiO_2 film appears.

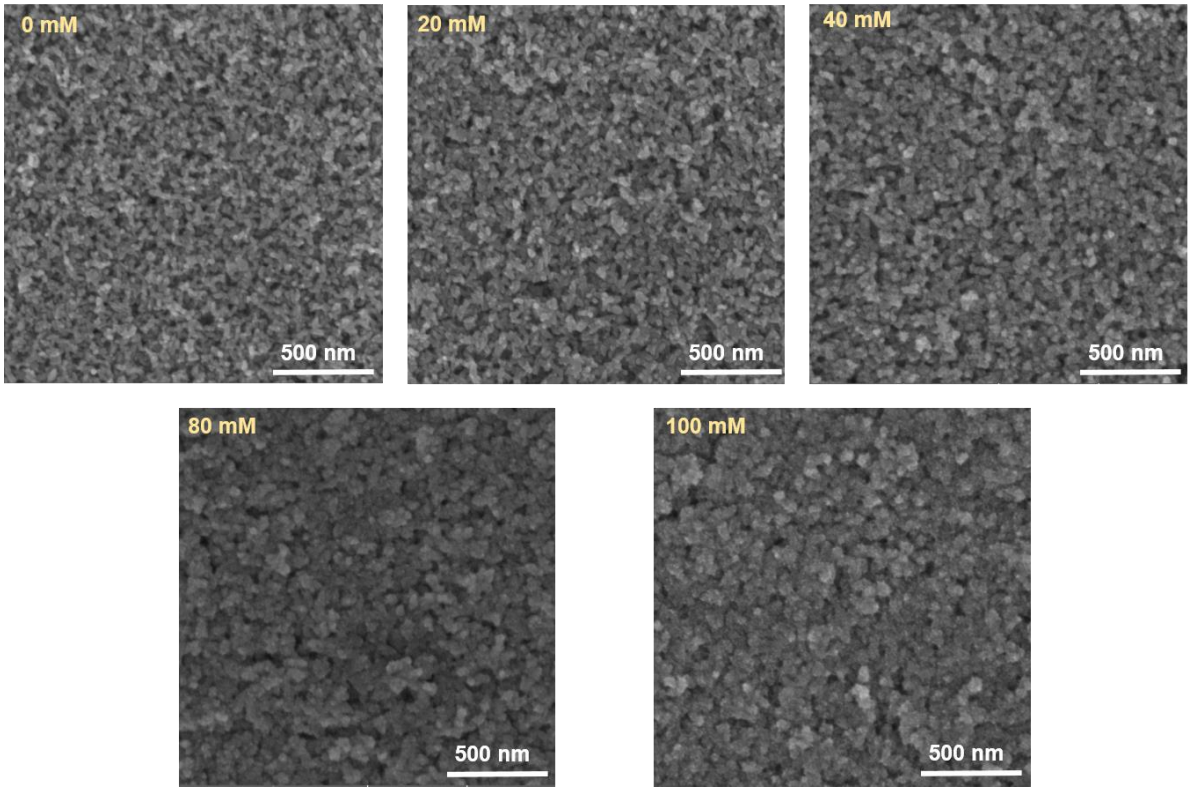

Figure 1: The top-view SEM images of the pristine mesoporous TiO_2 and mesoporous TiO_2 films post-treated in the aqueous $TiCl_4$ solution at different concentrations.

TiO_2 films were prepared for high-resolution electron imaging using a FEI Helios focused ion beam (FIB). The TEM imaging was performed using a FEI Titan^3 electron microscope operating at 300kV acceleration voltage. Tungsten (W) was deposited as a protection layer for the ion milling process and was used for the analysis of the changes in porosity of the deposited coatings.

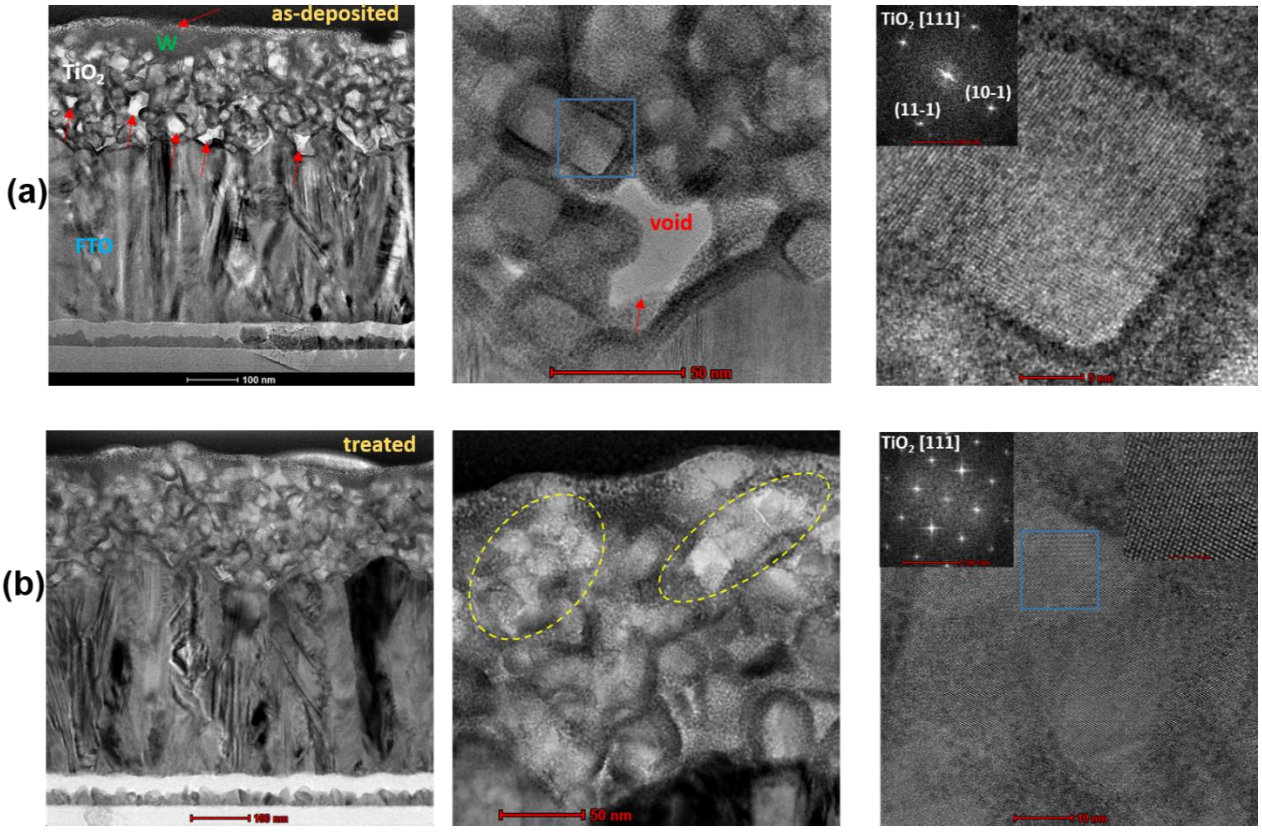

Figure 2: Cross-sectional SEM image and high resolution images of as deposited TiO_2 on FTO coated glass (a) and $TiCl_4$ treated (80 mM) TiO_2 on FTO coated glass (b).

Figure 2 (a) shows the structure of the as-deposited mesoporousTiO_2 coating on FTO coated glass and high-resolution images of the mesoporous TiO_2 film with crystallite size between 10 and 50 nm. The TiO_2 structure is identified as tetragonal anatase. Voids are observed through the

nanostructure of the film and at the top interface of the coating as shown by arrows in Figure 2(a). The surface irregularities and most of the interstitial space between the TiO_2 grains are replaced by the W deposited as a protection film for the ion beam preparation. Figure S2 shows a high-angle annular dark field (HAADF) image of the TiO_2 deposited on FTO, the associated EDX maps and spectrum acquired for the mesoporous coating. Large intrusions of W are observed at the top interface of the porous. The deposited W is found throughout the thickness of the film filling the porous structure. Oxygen is concentrated in the Ti-rich regions but it is also found in the interstitial spaces where it reacts with W. The results of the quantitative analysis performed on the as-deposited film are displayed in Table S1.

For the $TiCl_4$ treated (80 mM) TiO_2 sample, the overall microstructure remains unchanged. As shown in Figure 2(b), fewer voids are seen along the length of the coating which has a more compact appearance. The nanostructure of the film remains unchanged with the exception of large coalesced structures measuring close to 100nm in diameter which are observed. The oxide is identified as nanocrystalline anatase as shown in the high-resolution image. As shown in Figure S3, the treated TiO_2 forms a more compact structure with a decreased size and density of structural voids. The chemical analysis results (Table S2) show a drop in interstitial W concentration by a factor 2 pointing towards the formation of a denser TiO_2 coating. Such improved morphology is due to the fact that the $TiCl_4$ treatment results in the deposition of conformal TiO_2 layer on the surface of the TiO_2 particles, leading to an improvement in interconnection between these particles (percolation) and a smoother surface, facilitating charge transport to electrode. The formation of large coalesced structures also reduced the size and density of structural voids in the mesoporusTiO_2 film, thereby reducing the charge recombination

at grain boundaries. The XRD patterns of pristine and $TiCl_4$ treated mesoporous TiO_2 are shown in Figure S4 together with peak assignments. All the samples show similar anatase crystalline phase of TiO_2. In contrast, there was still a small amount of brookite phase (~ 5 wt%) in the pristine mesoporous TiO_2 film, as evidenced by the diffraction peak at 31.65° (211). It is clear that the $TiCl_4$ treatment improved the anatase crystallinity of the TiO_2 mesoporous layer compared to the pristine material.

The surface morphology of the perovskite films has a substantial influence on the photovoltaic performance of PSCs. The top-view SEM images of the perovskite films deposited on pristine and various concentration $TiCl_4$ treated mesoporous TiO_2 substrates are shown in Figure 3. All the perovskite films exhibited pinhole-free surface morphology with similar grain sizes. However, perovskite films grown on $TiCl_4$ treated mesoporous TiO_2 with concentration up to 80 mM showed a denser and much more homogeneous surface morphology compared to the perovskite film on pristine mesoporous TiO_2. With further increase of the concentration to 100 mM, the surface morphology of the perovskite films became non-uniform. Consequently, it indicates that the morphology of the perovskite films was strongly influenced by the morphology of the TiO_2 substrates. A homogeneous flat perovskite film can improve contact with HTL, thus decreasing the interface resistance and facilitating the charge transport[47].

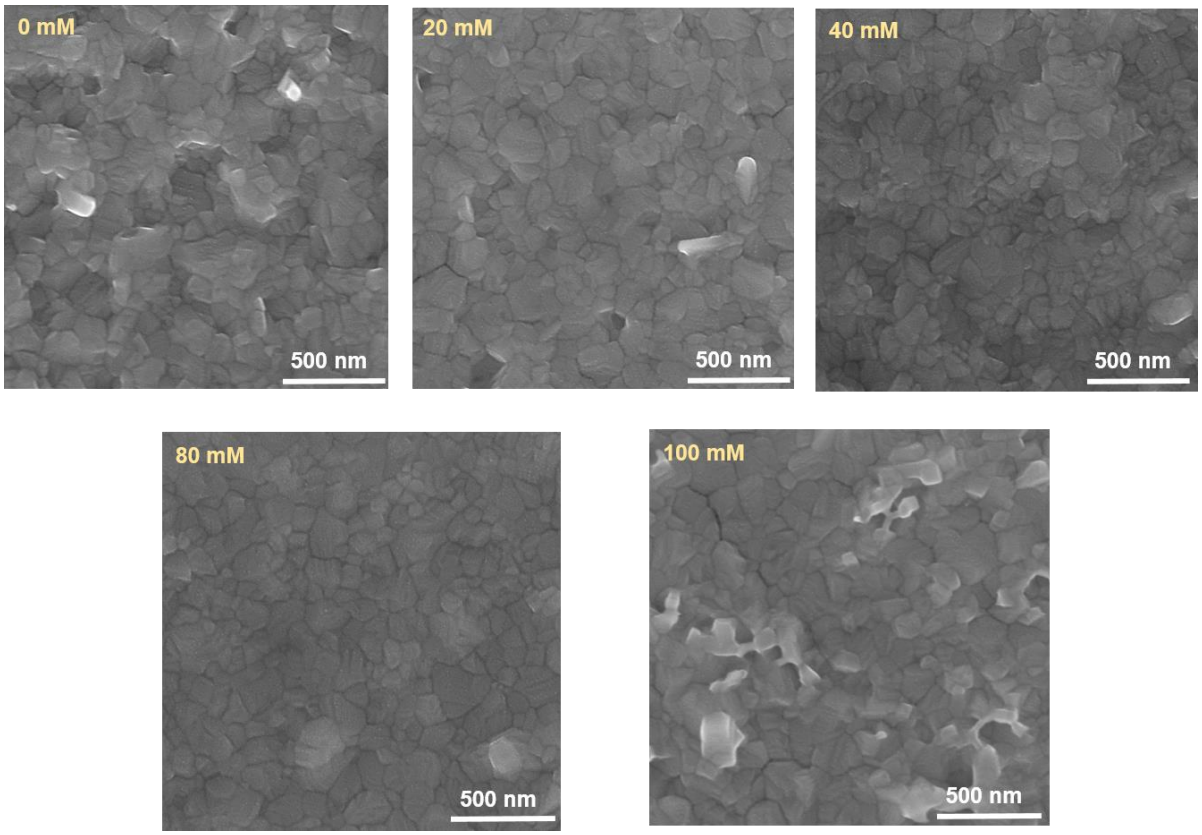

Figure 3: The top-view SEM images of the perovskite films deposited on pristine and $TiCl_4$-treated mesoporous TiO_2 substrates for various concentrations of $TiCl_4$.

PDS measurements were performed to scrutinize the effect of $TiCl_4$ treatment with various concentrations on trap states in mesoporous TiO_2 films. Figure 4(a) shows the PDS absorptance spectra of pristine and mesoporous TiO_2 films post-treated in the aqueous $TiCl_4$ solution at different concentrations. It can be seen that $TiCl_4$ treatment results in a significant reduction in sub-bandgap absorption and an increase in the density of states near the band edge in mesoporous TiO_2 films, which can potentially facilitate the charge transport within the mesoporous film in a device. An exponential tail in the absorption coefficient at the absorption edge is termed an Urbach Tail[48]. The slope of this sub-bandgap absorption edge varies with the

degree of electronic disorder within the material and is characterized by the Urbach energy E_U as in equation 1:[2, 49]

$$\alpha(E) \propto exp\left(\frac{E}{E_U}\right) \qquad (1)$$

where α is the absorption coefficient and E is the photon energy. The estimated Urbach energies for pristine and $TiCl_4$ treated mesoporous TiO_2 films are shown in Figure 4(b) and are 108.5, 106.6, 91.8, 82.8, and 96.6 meV for pristine, 20, 40, 80, and 100 mM $TiCl_4$ treated mesoporous TiO_2, respectively. The fitting of absorption coefficient data to determine the Urbach energies is shown in Figure S5. The $TiCl_4$ treatment resulted in a gradual reduction in E_U up to 80 mM $TiCl_4$ concentration, followed by an increase for higher $TiCl_4$ concentration. The $TiCl_4$-treated mesoporous TiO_2 (80 mM) has the lowest E_U (82.8 meV), indicating the lowest level of electronic disorder among these samples.

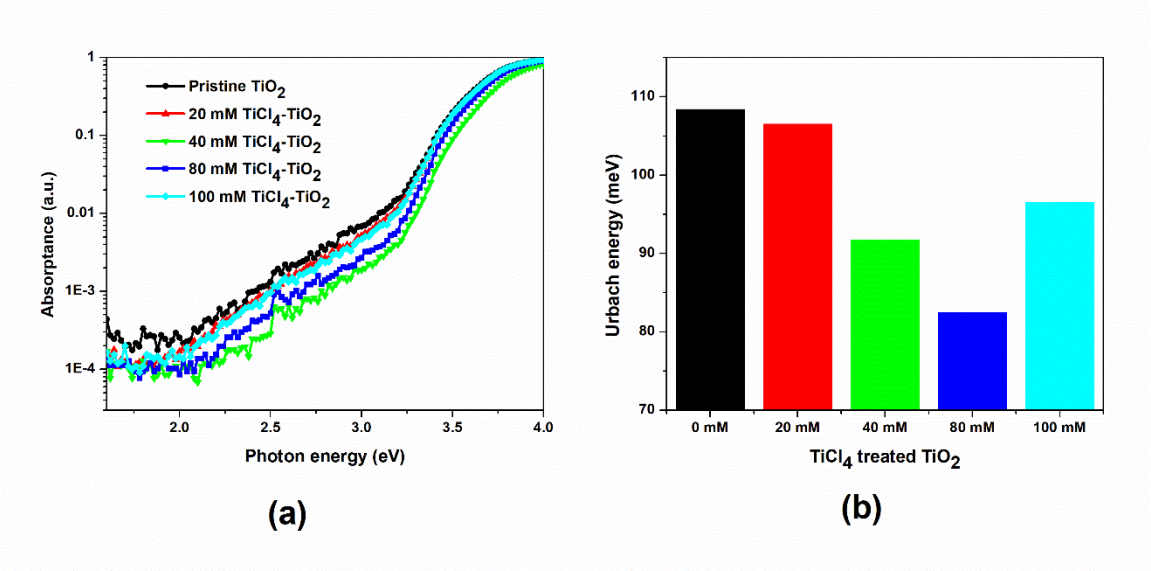

Figure 4: (a) PDS absorptance spectra and (b) estimated Urbach energy of pristine and $TiCl_4$ treated mesoporous TiO_2 ($TiCl_4$-TiO_2) substrates with various concentrations.

The impact of $TiCl_4$ treated mesoporous TiO_2 with various concentrations on the photovoltaic performance of PSCs was explored by measuring current density-voltage (J-V) curves under simulated AM 1.5G (100 mW cm^{-2}) solar illumination. In this study, mesoscopic PSCs were fabricated with the FTO/compact-TiO_2/mesoporous TiO_2/$CH_3NH_3PbI_3$ perovskite/Spiro-OMeTAD/Au device structure shown in Figure 5(a). The J-V characteristics of the best performing PSC devices based on pristine and $TiCl_4$-treated mesoporous TiO_2 with various concentrations are shown in Figure 5(b). The corresponding photovoltaic parameters are summarized in Table 1. As shown in Figure 5(b) and Table 1, a continuous increase in PCE is observed with increasing the $TiCl_4$ concentration up to 80 mM. However, further increasing the $TiCl_4$ concentration to 100 mM results in a decrease of PCE. It is evident that there is an optimum $TiCl_4$ concentration for the best device performance at 80 mM. The champion device based on 80 mM $TiCl_4$-treated mesoporous TiO_2 exhibited an open circuit voltage (V_{OC}) of 1.085 V, a short circuit current density (J_{SC}) of 22.9 $mAcm^{-2}$, and a fill factor (FF) of 70%, achieving an overall PCE of 17.4%. This represents a significantly improved performance compared to the PSC device with a pristine mesoporous TiO_2 ETL, which showed a PCE of 14.1% with a V_{OC} of 1.010 V, a J_{SC} of 21.3 $mAcm^{-2}$, and a FF of 65.7 %.

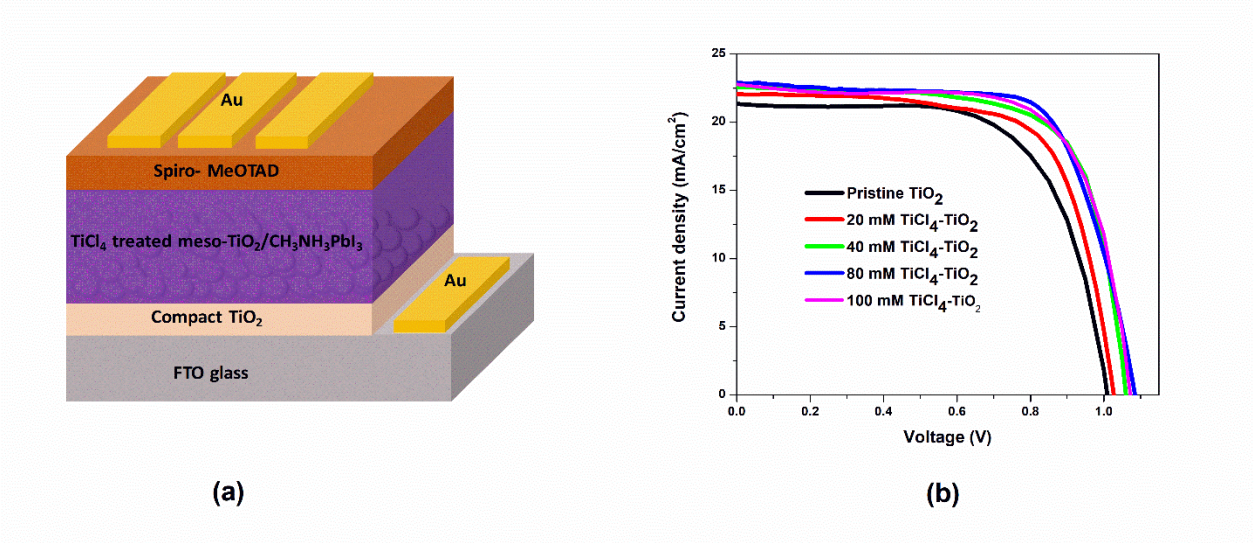

Figure 5: (a) Schematic illustration of n-i-p mesoscopic perovskite solar cell architecture and (b) current density-voltage (J-V) characteristics of the perovskite solar cells fabricated on pristine and $TiCl_4$ treated mesoporous TiO_2 substrates with various concentrations.

Table 1: Summary of photovoltaic parameters extracted from the J-V measurements of best-performing perovskite solar cells fabricated on pristine and $TiCl_4$ treated mesoporous TiO_2 substrates with various concentrations.

Sample name	V_{OC} (V)	J_{SC} (mA/cm^2)	FF (%)	PCE (%)
Pristine TiO_2	1.010	21.3	65.7	14.1
20 mM $TiCl_4$-TiO_2	1.027	22.1	68.9	15.6
40 mM $TiCl_4$-TiO_2	1.060	22.6	70.0	16.8
80 mM $TiCl_4$-TiO_2	1.085	22.9	70.0	17.4
100 mM $TiCl_4$-TiO_2	1.072	22.8	69.4	17.0

To determine more precisely the influence of $TiCl_4$ treated mesoporous TiO_2 with various concentrations on the photovoltaic performance, a set of twelve devices for each type (pristine,

20, 40, 80, and 100 mM) were fabricated and characterized. The detailed distribution box plots of photovoltaic parameters of the PSCs based on pristine and $TiCl_4$ treated mesoporous TiO_2 with various doping concentrations derived from reverse scan measurements are shown in Figure S6, and average values are listed in Table S3. The average PCE of the PSCs was significantly increased from 13.3% to 16.8% with increasing $TiCl_4$ concentration up to 80 mM. However, with further increase in the $TiCl_4$ concentration to 100 mM, the average PCE of the PSCs decreased to 16.2%. It is evident that $TiCl_4$ treatment substantially enhanced device reproducibility and consistency.

The external quantum efficiency (EQE) of the devices based on pristine and 80 mM $TiCl_4$ treated mesoporous TiO_2 was measured to confirm the improvement in J_{SC}. Figure 6 (a) shows the EQE spectra and integrated J_{SC} for the best performing cells. The 80 mM $TiCl_4$ treated mesoporous TiO_2 based PSC exhibits higher EQE than the pristine mesoporous TiO_2 based cell over the entire responsive range of wavelengths, though the improvement is reduced in the UV range. This indicates that the cell with optimized contact still has limited collection of holes that are generated close to the front contact. The integrated J_{SC} values from EQE curves for the devices based on pristine and 80 mM $TiCl_4$ treated mesoporous TiO_2 are 20.2 $mAcm^{-2}$ and 21.9 $mAcm^{-2}$, respectively, fairly consistent with the corresponding J_{SC} values obtained from J-V results (within 5% deviation). A significant improvement in V_{OC}, J_{SC}, and FF after $TiCl_4$ treatment can be attributed to an efficient charge extraction/collection and suppressed charge recombination at the interface owing to the improvement in interconnection between the TiO_2 particles, the significant reduction in sub-bandgap absorption, and a lower level of electronic disorder in the mesoporous TiO_2 films[46, 50].

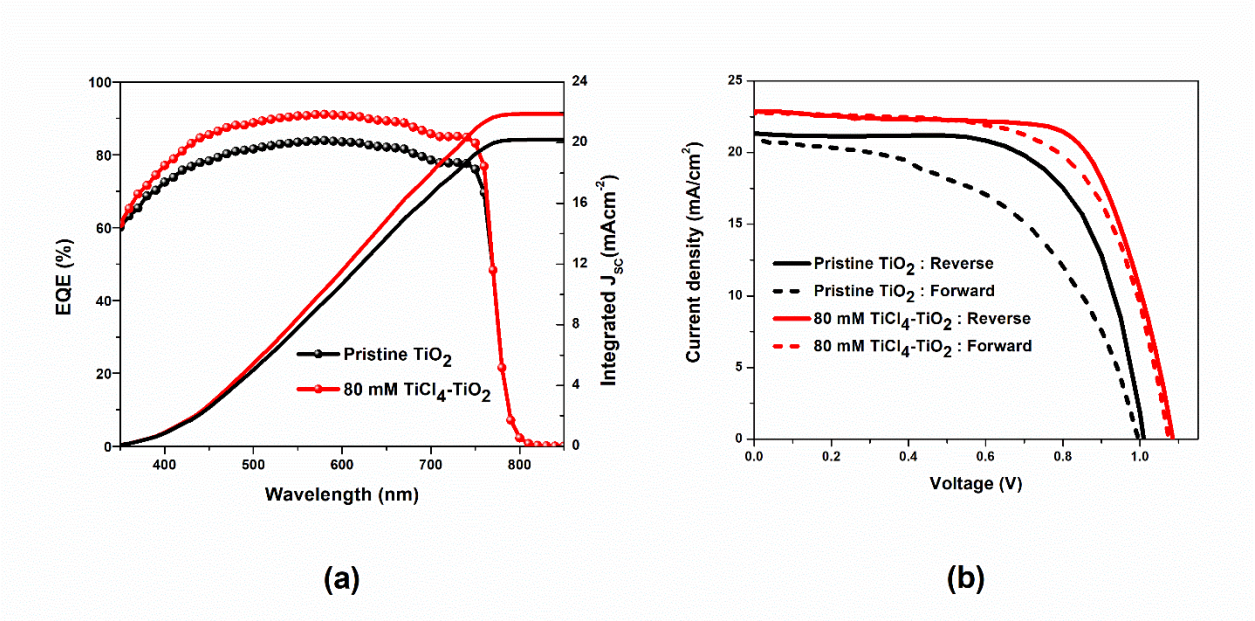

Figure 6: (a) External quantum efficiency (EQE) spectra and integrated J_{SC} for the pristine and 80 mM $TiCl_4$ treated mesoporous TiO_2 based devices and (b) J-V characteristics of best performing devices based on pristine and 80 mM $TiCl_4$ treated mesoporous TiO_2 under reverse and forward scan conditions.

The J-V hysteresis behavior is a well-known phenomenon in which the shapes of J–V curves vary depending on the scan direction, rate, and range of the scan voltage [51] during the measurements of PSCs due to the ferroelectric effect [52], unbalanced charge carrier transport [53], ion and vacancy migration [54-55], and trap-assisted charge recombination[56]. The hysteresis can be quantitatively described by a hysteresis index (HI), which is often defined by the PCE in various scan directions according to equation 2, where $PCE_{reverse}$ and $PCE_{forward}$ are power conversion efficiency from reverse and forward scan, respectively [57].

$$HI\ (\%) = \frac{PCE_{reverse} - PCE_{forward}}{PCE_{reverse}} \times 100 \qquad (2)$$

Typical J-V curves for the PSCs based on pristine and 80 mM $TiCl_4$ treated mesoporous TiO_2 are shown in Figure 6(b) with reverse and forward scan directions shown to estimate the J–V hysteresis. The corresponding photovoltaic parameters and HI are summarized in Table S4. The cell based on 80 mM $TiCl_4$ treated mesoporous TiO_2 exhibited a HI of 8.6%, much lower than that of the pristine mesoporous TiO_2 based cell (HI=24.8%). The enhanced interconnection between the TiO_2 particles, improved interfacial contact and reduced number of trap states after the $TiCl_4$ treatment as mentioned above can contribute to the improved charge extraction and transport abilities and decreased charge accumulation and recombination loss at TiO_2/perovskite interface, leading to reduced J–V hysteresis [36, 51, 57].

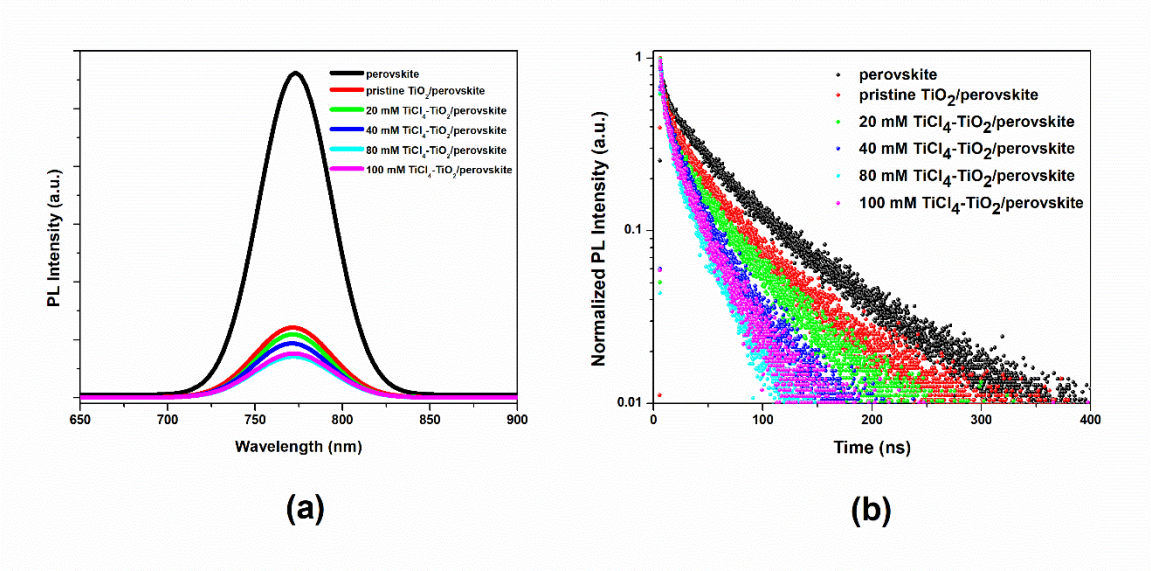

Figure 7: (a) Steady-state photoluminescence (PL) spectra and (b) normalized time-resolved photoluminescence (TRPL) decays of perovskite films deposited on glass, and mesoporous TiO_2 /glass samples treated with various $TiCl_4$ concentrations.

To gain insight into the charge carrier extraction and transport mechanism behind the enhancement in the device performance, steady-state PL and TRPL measurements were performed for perovskite films deposited on pristine and $TiCl_4$ treated mesoporous TiO_2 samples with various concentrations. As shown in Figure 7(a), it is found that the intensity of the PL peak at 770 nm for the perovskite film deposited on glass was significantly quenched when incorporating the pristine or $TiCl_4$ treated mesoporous TiO_2 between the perovskite film and glass. Compared to the perovskite film on pristine mesoporous TiO_2, the PL emission intensity was quenched more effectively for the perovskite films on $TiCl_4$ treated mesoporous TiO_2 samples and the strongest PL quenching is shown for the 80 mM $TiCl_4$ treated sample. Figure 7(b) shows the TRPL decays measured at the peak emission wavelength (770 nm) for the perovskite films deposited on pristine and $TiCl_4$ treated mesoporous TiO_2 samples with various concentrations. The corresponding fitted and calculated parameters are listed in Table S5. The average PL lifetime of the perovskite film on pristine mesoporous TiO_2 is significantly decreased compared to perovskite film deposited on glass, from 60.9 ns to 44.9 ns. It is further reduced to 21.3 ns when incorporating the $TiCl_4$ treated mesoporous TiO_2 with a concentration of up to 80 mM, followed by an increase (to 24.5 ns) for a higher $TiCl_4$ concentration (100 mM), which is consistent with steady-state PL observation. The strongest PL quenching and shortest PL lifetime in the perovskite film deposited on 80 mM $TiCl_4$ treated mesoporous TiO_2 demonstrates that the electron transfer dynamics are faster from perovskite to 80 mM $TiCl_4$ treated mesoporous TiO_2, which is favorable for efficient charge extraction and minimized charge recombination at the interface, resulting in a higher V_{OC} and J_{SC}, in accordance with the J-V results.

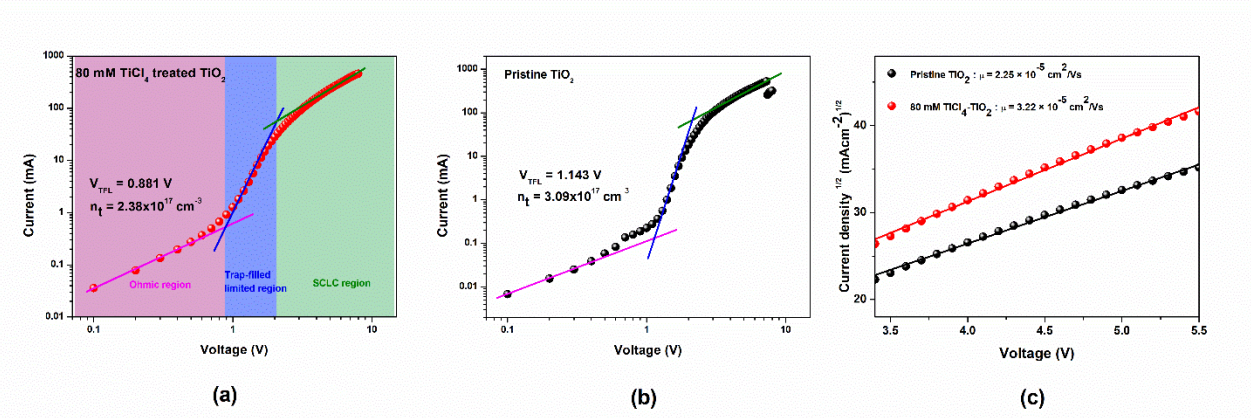

Figure 8: The double logarithmic I-V curves for (a) 80 mM $TiCl_4$ treated mesoporous TiO_2 and (b) pristine mesoporous TiO_2 using the space-charge-limited current (SCLC) model with a device structure of FTO/TiO_2/Au and (c) $J^{1/2}$-V curves in a trap-free SCLC region fit with Mott-Gurney law.

To gain further insight into the influence of $TiCl_4$ treatment on defect density and mobility of TiO_2 films, a space-charge-limited current (SCLC) measurement was performed. Figure 8 (a) and (b) show the I-V curves of the electron-only devices measured under dark conditions and plotted on a double logarithmic plot for 80 mM $TiCl_4$ treated and pristine mesoporous TiO_2, respectively. As shown in Figure 8(a), the dark I-V curve shows three regions of behavior: an Ohmic region at low bias voltage, a trap-filled limited region at an intermediate bias voltage and a trap free SCLC region at higher bias voltage. A linear relation represents an Ohmic response at a low bias voltage. The current suddenly increases nonlinearly and much more rapidly as bias voltage increases, demonstrating the trap-filled limited region. The transition point between the Ohmic and trap-filled limited region is recognized as the trap-filled limit voltage (V_{TFL}). The trap density (n_t) is estimated according to equation 3:

$$n_t = \frac{2\varepsilon_r\varepsilon_0 V_{TFL}}{eL^2} \qquad (3)$$

where ε_r is the dielectric constant of anatase TiO_2, ε_0 is the vacuum permittivity, e is the elementary charge of the electron, and L is the thickness of the TiO_2 film [58-59]. The V_{TFL} was obtained from the transition kink point for 80 mM $TiCl_4$ treated and pristine mesoporous TiO_2 as shown in Figure 8 (a) and (b), respectively. The V_{TFL} of device based 80 mM $TiCl_4$ treated mesoporous TiO_2 (0.881 V) is lower than that of pristine mesoporous TiO_2 (1.143 V). Thus, the estimated electron trap density of 80 mM $TiCl_4$ treated mesoporous TiO_2 is 2.38×10^{17} cm^{-3}, lower than that of pristine mesoporous TiO_2, at 3.09×10^{17} cm^{-3}. This is further evidence that $TiCl_4$ treatment reduces the number of trap states, which is in agreement with increased V_{OC} and FF. In addition, the electron mobility of the pristine and 80 mM $TiCl_4$ treated mesoporous TiO_2 can be calculated by fitting the J-V curves of the electron only devices in the trap free SCLC region as shown in Figure 8(C) using the Mott-Gurney law according to equation 4 [60-61]

$$J = \frac{9}{8}\mu\varepsilon_r\varepsilon_0\frac{V^2}{L^3} \qquad (4)$$

where J is the current density, μ is the electron mobility, V is the applied voltage, and L is the thickness of mesoporous TiO_2. The calculated electron mobility of 80 mM $TiCl_4$ treated mesoporous TiO_2 (3.22×10^{-5} $cm^2V^{-1}s^{-1}$) is higher than that of pristine mesoporous TiO_2 (2.25×10^{-5} $cm^2V^{-1}s^{-1}$), demonstrating that $TiCl_4$ treatment can efficiently improve the electron transport within TiO_2 film, which is in agreement with increased J_{SC}. The additional interconnection between the TiO_2 particles, lower number of trap states and higher electron mobility after $TiCl_4$ treatment all contribute to improved charge transport and suppressed charge recombination in solar cells, resulting in an overall enhancement in the PCE. Moreover, superior charge transport and

suppressed recombination contribute to decreased charge accumulation at the interface, resulting in reduced J–V hysteresis.

Conclusions

We have systematically investigated the role of $TiCl_4$ treatment on mesoporous TiO_2 layer in $CH_3NH_3PbI_3$ perovskite solar cells by varying the concentrations of $TiCl_4$. It is found that $TiCl_4$ treatment led to an improvement in interconnection between the TiO_2 particles, decreased the number of trap states and increased the electron mobility, which improved charge extraction, decreased the charge accumulation and recombination loss at the TiO_2/perovskite interface. Consequently, a significant enhancement in the V_{OC}, J_{SC}, and FF of devices with $TiCl_4$ treated mesoporous TiO_2 was observed along with reduced hysteresis as compared to device with pristine mesoporous TiO_2. A solar cell with an optimized treatment by 80 mM concentration of $TiCl_4$ shows the highest efficiency of 17.4 %, compared with a champion efficiency of 14.1 % for a device with pristine mesoporous TiO_2 layer.

Supporting Information

The lower magnification SEM images of TiO_2 films, dark field imaging and chemical maps of as-deposited and treated mesoporous TiO_2, XRD patterns of TiO_2 films, Fittings of PDS data for Urbach energy of TiO_2 films, box-charts of the photovoltaic parameters, the average photovoltaic parameters of the PSC devices with various doping concentrations, the photovoltaic parameters measured under reverse- and forward-scan directions, and fitted parameters of the TRPL spectra are provided in the supporting information.

Conflicts of interest

The authors declare no conflict of interest.

Acknowledgments

This work was supported by the Czech Ministry of Education, Youth and Sports project (CZ. 02.1.01/0.0/0.0/15_003/0000464 - Centre of Advanced Photovoltaics) and Czech Science Foundation grant no 18-24268S. L.H acknowledges support from Czech Ministry of Education, Youth and Sports: project CZ.02.1.01/0.0/0.0/15_003/0000485. Part of the work was carried out with the support of CEITEC Nano Research Infrastructure (ID LM2015041, MEYS CR, 2016–2019), CEITEC Brno University of Technology.

References

1. Eperon, G. E.; Stranks, S. D.; Menelaou, C.; Johnston, M. B.; Herz, L. M.; Snaith, H. J. Formamidinium Lead Trihalide: A Broadly Tunable Perovskite for Efficient Planar Heterojunction Solar Cells. *Energy Environ. Sci.* **2014**, *7*, 982-988.

2. De Wolf, S.; Holovsky, J.; Moon, S.-J.; Löper, P.; Niesen, B.; Ledinsky, M.; Haug, F.-J.; Yum, J.-H.; Ballif, C. Organometallic Halide Perovskites: Sharp Optical Absorption Edge and Its Relation to Photovoltaic Performance. *J. Phys. Chem. Lett.* **2014**, *5*, 1035-1039.

3. Stranks, S. D.; Eperon, G. E.; Grancini, G.; Menelaou, C.; Alcocer, M. J.; Leijtens, T.; Herz, L. M.; Petrozza, A.; Snaith, H. J. Electron-Hole Diffusion Lengths Exceeding 1 Micrometer in an Organometal Trihalide Perovskite Absorber. *Science* **2013**, *342*, 341-344.

4. Filip, M. R.; Eperon, G. E.; Snaith, H. J.; Giustino, F. Steric Engineering of Metal-Halide Perovskites with Tunable Optical Band Gaps. *Nat. Commun.* **2014**, *5*, 5757.

5. Lim, J.; Hörantner, M. T.; Sakai, N.; Ball, J. M.; Mahesh, S.; Noel, N. K.; Lin, Y.-H.; Patel, J. B.; McMeekin, D. P.; Johnston, M. B. Elucidating the Long-Range Charge Carrier Mobility in Metal Halide Perovskite Thin Films. *Energy Environ. Sci.* **2019**, *12*, 169-176.

6. Pazos-Outón, L. M.; Szumilo, M.; Lamboll, R.; Richter, J. M.; Crespo-Quesada, M.; Abdi-Jalebi, M.; Beeson, H. J.; Vrućinić, M.; Alsari, M.; Snaith, H. J. Photon Recycling in Lead Iodide Perovskite Solar Cells. *Science* **2016**, *351*, 1430-1433.

7. Kojima, A.; Teshima, K.; Shirai, Y.; Miyasaka, T. Organometal Halide Perovskites as Visible-Light Sensitizers for Photovoltaic Cells. *J. Am. Chem. Soc.* **2009**, *131*, 6050-6051.

8. Kim, H.-S.; Lee, C.-R.; Im, J.-H.; Lee, K.-B.; Moehl, T.; Marchioro, A.; Moon, S.-J.; Humphry-Baker, R.; Yum, J.-H.; Moser, J. E. Lead Iodide Perovskite Sensitized All-Solid-State Submicron Thin Film Mesoscopic Solar Cell with Efficiency Exceeding 9%. *Sci. Rep.* **2012**, *2*, 591.

9. Lee, M. M.; Teuscher, J.; Miyasaka, T.; Murakami, T. N.; Snaith, H. J. Efficient Hybrid Solar Cells Based on Meso-Superstructured Organometal Halide Perovskites. *Science* **2012**, *338*, 643-647.

10. NREL Best Research-Cell Efficiency Chart. https://www.nrel.gov/pv/cell-efficiency.html (accessed 11/11/2019).

11. You, J.; Meng, L.; Song, T.-B.; Guo, T.-F.; Yang, Y. M.; Chang, W.-H.; Hong, Z.; Chen, H.; Zhou, H.; Chen, Q. Improved Air Stability of Perovskite Solar Cells Via Solution-Processed Metal Oxide Transport Layers. *Nat. Nanotechnol.* **2016**, *11*, 75.

12. Zhang, H.; Shi, J.; Xu, X.; Zhu, L.; Luo, Y.; Li, D.; Meng, Q. Mg-Doped Tio2 Boosts the Efficiency of Planar Perovskite Solar Cells to Exceed 19%. *J. Mater. Chem. A* **2016**, *4*, 15383-15389.

13. Li, W.; Zhang, W.; Van Reenen, S.; Sutton, R. J.; Fan, J.; Haghighirad, A. A.; Johnston, M. B.; Wang, L.; Snaith, H. J. Enhanced Uv-Light Stability of Planar Heterojunction Perovskite Solar Cells with Caesium Bromide Interface Modification. *Energy Environ. Sci.* **2016**, *9*, 490-498.

14. Etgar, L.; Gao, P.; Xue, Z.; Peng, Q.; Chandiran, A. K.; Liu, B.; Nazeeruddin, M. K.; Grätzel, M. Mesoscopic Ch3nh3pbi3/Tio2 Heterojunction Solar Cells. *J. Am. Chem. Soc.* **2012**, *134*, 17396-17399.

15. Peter Amalathas, A.; Landová, L.; Conrad, B.; Holovský, J. Concentration-Dependent Impact of Alkali Li Metal Doped Mesoporous Tio2 Electron Transport Layer on the Performance of Ch3nh3pbi3 Perovskite Solar Cells. *J. Phys. Chem. C* **2019**, *123*, 19376-19384.

16. Cao, J.; Wu, B.; Chen, R.; Wu, Y.; Hui, Y.; Mao, B. W.; Zheng, N. Efficient, Hysteresis-Free, and Stable Perovskite Solar Cells with Zno as Electron-Transport Layer: Effect of Surface Passivation. *Adv. Mater.* **2018**, *30*, 1705596.

17. Zhang, P.; Wu, J.; Zhang, T.; Wang, Y.; Liu, D.; Chen, H.; Ji, L.; Liu, C.; Ahmad, W.; Chen, Z. D. Perovskite Solar Cells with Zno Electron-Transporting Materials. *Adv. Mater.* **2018**, *30*, 1703737.

18. Zhu, Z.; Bai, Y.; Liu, X.; Chueh, C. C.; Yang, S.; Jen, A. K. Y. Enhanced Efficiency and Stability of Inverted Perovskite Solar Cells Using Highly Crystalline Sno2 Nanocrystals as the Robust Electron-Transporting Layer. *Adv. Mater.* **2016**, *28*, 6478-6484.

19. Roose, B.; Baena, J.-P. C.; Gödel, K. C.; Graetzel, M.; Hagfeldt, A.; Steiner, U.; Abate, A. Mesoporous Sno2 Electron Selective Contact Enables Uv-Stable Perovskite Solar Cells. *Nano Energy* **2016**, *30*, 517-522.

20. Kogo, A.; Numata, Y.; Ikegami, M.; Miyasaka, T. Nb2o5 Blocking Layer for High Open-Circuit Voltage Perovskite Solar Cells. *Chem. Lett.* **2015**, *44*, 829-830.

21. Bera, A.; Wu, K.; Sheikh, A.; Alarousu, E.; Mohammed, O. F.; Wu, T. Perovskite Oxide Srtio3 as an Efficient Electron Transporter for Hybrid Perovskite Solar Cells. *J. Phys. Chem. C* **2014**, *118*, 28494-28501.

22. Wei, J.; Guo, F.; Liu, B.; Sun, X.; Wang, X.; Yang, Z.; Xu, K.; Lei, M.; Zhao, Y.; Xu, D. Uv-Inert Zntio3 Electron Selective Layer for Photostable Perovskite Solar Cells. *Adv. Energy Mater.* **2019**.

23. Bera, A.; Sheikh, A. D.; Haque, M. A.; Bose, R.; Alarousu, E.; Mohammed, O. F.; Wu, T. Fast Crystallization and Improved Stability of Perovskite Solar Cells with Zn2sno4 Electron Transporting Layer: Interface Matters. *ACS Appl. Mater. Interfaces* **2015**, *7*, 28404-28411.

24. Wang, K.; Shi, Y.; Dong, Q.; Li, Y.; Wang, S.; Yu, X.; Wu, M.; Ma, T. Low-Temperature and Solution-Processed Amorphous Wo X as Electron-Selective Layer for Perovskite Solar Cells. *J. Phys. Chem. Lett.* **2015**, *6*, 755-759.

25. Qin, M.; Ma, J.; Ke, W.; Qin, P.; Lei, H.; Tao, H.; Zheng, X.; Xiong, L.; Liu, Q.; Chen, Z. Perovskite Solar Cells Based on Low-Temperature Processed Indium Oxide Electron Selective Layers. *ACS Appl. Mater. Interfaces* **2016**, *8*, 8460-8466.

26. Shin, S. S.; Yeom, E. J.; Yang, W. S.; Hur, S.; Kim, M. G.; Im, J.; Seo, J.; Noh, J. H.; Seok, S. I. Colloidally Prepared La-Doped Basno3 Electrodes for Efficient, Photostable Perovskite Solar Cells. *Science* **2017**, *356*, 167-171.

27. Wang, X.; Deng, L.-L.; Wang, L.-Y.; Dai, S.-M.; Xing, Z.; Zhan, X.-X.; Lu, X.-Z.; Xie, S.-Y.; Huang, R.-B.; Zheng, L.-S. Cerium Oxide Standing out as an Electron Transport Layer for Efficient and Stable Perovskite Solar Cells Processed at Low Temperature. *J. Mater. Chem. A* **2017**, *5*, 1706-1712.

28. Min, H.; Kim, M.; Lee, S.-U.; Kim, H.; Kim, G.; Choi, K.; Lee, J. H.; Seok, S. I. Efficient, Stable Solar Cells by Using Inherent Bandgap of A-Phase Formamidinium Lead Iodide. *Science* **2019**, *366*, 749-753.

29. Jung, E. H.; Jeon, N. J.; Park, E. Y.; Moon, C. S.; Shin, T. J.; Yang, T.-Y.; Noh, J. H.; Seo, J. Efficient, Stable and Scalable Perovskite Solar Cells Using Poly (3-Hexylthiophene). *Nature* **2019**, *567*, 511.

30. Yang, W. S., et al. Iodide Management in Formamidinium-Lead-Halide-Based Perovskite Layers for Efficient Solar Cells. *Science* **2017**, *356*, 1376-1379.

31. Jeon, N. J.; Na, H.; Jung, E. H.; Yang, T.-Y.; Lee, Y. G.; Kim, G.; Shin, H.-W.; Il Seok, S.; Lee, J.; Seo, J. A Fluorene-Terminated Hole-Transporting Material for Highly Efficient and Stable Perovskite Solar Cells. *Nat. Energy* **2018**, *3*, 682-689.

32. Li, Y.; Zhao, Y.; Chen, Q.; Yang, Y.; Liu, Y.; Hong, Z.; Liu, Z.; Hsieh, Y.-T.; Meng, L.; Li, Y. Multifunctional Fullerene Derivative for Interface Engineering in Perovskite Solar Cells. *J. Am. Chem. Soc.* **2015**, *137*, 15540-15547.

33. Liu, X.; Liu, Z.; Sun, B.; Tan, X.; Ye, H.; Tu, Y.; Shi, T.; Tang, Z.; Liao, G. 17.46% Efficient and Highly Stable Carbon-Based Planar Perovskite Solar Cells Employing Ni-Doped Rutile Tio2 as Electron Transport Layer. *Nano energy* **2018**, *50*, 201-211.

34. Wojciechowski, K.; Stranks, S. D.; Abate, A.; Sadoughi, G.; Sadhanala, A.; Kopidakis, N.; Rumbles, G.; Li, C.-Z.; Friend, R. H.; Jen, A. K.-Y. Heterojunction Modification for Highly Efficient Organic–Inorganic Perovskite Solar Cells. *ACS nano* **2014**, *8*, 12701-12709.

35. Shih, Y.-C.; Wang, L.; Hsieh, H.-C.; Lin, K.-F. Enhancing the Photocurrent of Perovskite Solar Cells Via Modification of the Tio 2/Ch 3 Nh 3 Pbi 3 Heterojunction Interface with Amino Acid. *J. Mater. Chem. A* **2015**, *3*, 9133-9136.

36. Sidhik, S.; Cerdan Pasarán, A.; Esparza, D.; Lopez Luke, T.; Carriles, R. n.; De la Rosa, E. Improving the Optoelectronic Properties of Mesoporous Tio2 by Cobalt Doping for High-Performance Hysteresis-Free Perovskite Solar Cells. *ACS Appl. Mater. Interfaces* **2018**, *10*, 3571-3580.

37. Zhu, Z.; Ma, J.; Wang, Z.; Mu, C.; Fan, Z.; Du, L.; Bai, Y.; Fan, L.; Yan, H.; Phillips, D. L. Efficiency Enhancement of Perovskite Solar Cells through Fast Electron Extraction: The Role of Graphene Quantum Dots. *J. Am. Chem. Soc.* **2014**, *136*, 3760-3763.

38. Cao, J.; Yin, J.; Yuan, S.; Zhao, Y.; Li, J.; Zheng, N. Thiols as Interfacial Modifiers to Enhance the Performance and Stability of Perovskite Solar Cells. *Nanoscale* **2015**, *7*, 9443-9447.

39. Kim, H. B.; Im, I.; Yoon, Y.; Do Sung, S.; Kim, E.; Kim, J.; Lee, W. I. Enhancement of Photovoltaic Properties of Ch 3 Nh 3 Pbbr 3 Heterojunction Solar Cells by Modifying Mesoporous Tio 2 Surfaces with Carboxyl Groups. *J. Mater. Chem. A* **2015**, *3*, 9264-9270.

40. Cojocaru, L.; Uchida, S.; Sanehira, Y.; Nakazaki, J.; Kubo, T.; Segawa, H. Surface Treatment of the Compact Tio2 Layer for Efficient Planar Heterojunction Perovskite Solar Cells. *Chem. Lett.* **2015**, *44*, 674-676.

41. Sommeling, P.; O'Regan, B. C.; Haswell, R.; Smit, H.; Bakker, N.; Smits, J.; Kroon, J. M.; Van Roosmalen, J. Influence of a Ticl4 Post-Treatment on Nanocrystalline Tio2 Films in Dye-Sensitized Solar Cells. *J. Phys. Chem. B* **2006**, *110*, 19191-19197.

42. O'Regan, B. C.; Durrant, J. R.; Sommeling, P. M.; Bakker, N. J. Influence of the Ticl4 Treatment on Nanocrystalline Tio2 Films in Dye-Sensitized Solar Cells. 2. Charge Density, Band Edge Shifts, and Quantification of Recombination Losses at Short Circuit. *J. Phys. Chem. C* **2007**, *111*, 14001-14010.

43. Zhao, J.; Wang, P.; Wei, L.; Liu, Z.; Fang, X.; Liu, X.; Ren, D.; Mai, Y. Efficient Charge-Transport in Hybrid Lead Iodide Perovskite Solar Cells. *Dalton Trans.* **2015**, *44*, 16914-22.

44. Liu, Z.; Chen, Q.; Hong, Z.; Zhou, H.; Xu, X.; De Marco, N.; Sun, P.; Zhao, Z.; Cheng, Y.-B.; Yang, Y. Low-Temperature Tio X Compact Layer for Planar Heterojunction Perovskite Solar Cells. *ACS Appl. Mater. Interfaces* **2016**, *8*, 11076-11083.

45. Murakami, T. N.; Miyadera, T.; Funaki, T.; Cojocaru, L.; Kazaoui, S.; Chikamatsu, M.; Segawa, H. Adjustment of Conduction Band Edge of Compact Tio2 Layer in Perovskite Solar Cells through Ticl4 Treatment. *ACS Appl. Mater. Interfaces* **2017**, *9*, 36708-36714.

46. Ma, J.; Chang, J.; Lin, Z.; Guo, X.; Zhou, L.; Liu, Z.; Xi, H.; Chen, D.; Zhang, C.; Hao, Y. Elucidating the Roles of Ticl4 and Pcbm Fullerene Treatment on Tio2 Electron Transporting Layer for Highly Efficient Planar Perovskite Solar Cells. *J. Phys. Chem. C* **2018**, *122*, 1044-1053.

47. Zhang, W.; Li, Y.; Liu, X.; Tang, D.; Li, X.; Yuan, X. Ethyl Acetate Green Antisolvent Process for High-Performance Planar Low-Temperature Sno2-Based Perovskite Solar Cells Made in Ambient Air. *Chem. Eng. J.* **2020**, *379*, 122298.

48. Urbach, F. The Long-Wavelength Edge of Photographic Sensitivity and of the Electronic Absorption of Solids. *Phys. Rev.* **1953**, *92*, 1324.

49. John, S.; Soukoulis, C.; Cohen, M. H.; Economou, E. Theory of Electron Band Tails and the Urbach Optical-Absorption Edge. *Phys. Rev. Lett.* **1986**, *57*, 1777.

50. Garmaroudi, Z. A.; Abdi-Jalebi, M.; Mohammadi, M. R.; Friend, R. H. A Facile Low Temperature Route to Deposit a Tio 2 Scattering Layer for Efficient Dye-Sensitized Solar Cells. *RSC Adv.* **2016**, *6*, 70895-70901.

51. Zhang, H.; Liang, C.; Zhao, Y.; Sun, M.; Liu, H.; Liang, J.; Li, D.; Zhang, F.; He, Z. Dynamic Interface Charge Governing the Current–Voltage Hysteresis in Perovskite Solar Cells. *Phys. Chem. Chem. Phys.* **2015**, *17*, 9613-9618.

52. Chen, B.; Zheng, X.; Yang, M.; Zhou, Y.; Kundu, S.; Shi, J.; Zhu, K.; Priya, S. Interface Band Structure Engineering by Ferroelectric Polarization in Perovskite Solar Cells. *Nano Energy* **2015**, *13*, 582-591.

53. Heo, J. H.; Han, H. J.; Kim, D.; Ahn, T. K.; Im, S. H. Hysteresis-Less Inverted Ch 3 Nh 3 Pbi 3 Planar Perovskite Hybrid Solar Cells with 18.1% Power Conversion Efficiency. *Energy Environ. Sci.* **2015**, *8*, 1602-1608.

54. Azpiroz, J. M.; Mosconi, E.; Bisquert, J.; De Angelis, F. Defect Migration in Methylammonium Lead Iodide and Its Role in Perovskite Solar Cell Operation. *Energy Environ. Sci.* **2015**, *8*, 2118-2127.

55. Eames, C.; Frost, J. M.; Barnes, P. R.; O'regan, B. C.; Walsh, A.; Islam, M. S. Ionic Transport in Hybrid Lead Iodide Perovskite Solar Cells. *Nat. Commun.* **2015**, *6*, 7497.

56. Aygüler, M. F.; Hufnagel, A. G.; Rieder, P.; Wussler, M.; Jaegermann, W.; Bein, T.; Dyakonov, V.; Petrus, M. L.; Baumann, A.; Docampo, P. Influence of Fermi Level Alignment with Tin Oxide on the Hysteresis of Perovskite Solar Cells. *ACS Appl. Mater. Interfaces* **2018**, *10*, 11414-11419.

57. Liu, P.; Wang, W.; Liu, S.; Yang, H.; Shao, Z. Fundamental Understanding of Photocurrent Hysteresis in Perovskite Solar Cells. *Adv. Energy Mater.* **2019**, 1803017.

58. Bube, R. H. Trap Density Determination by Space-Charge-Limited Currents. *J. Appl. Phys.* **1962**, *33*, 1733-1737.

59. Wu, M.-C.; Chan, S.-H.; Lee, K.-M.; Chen, S.-H.; Jao, M.-H.; Chen, Y.-F.; Su, W.-F. Enhancing the Efficiency of Perovskite Solar Cells Using Mesoscopic Zinc-Doped Tio2 as the Electron Extraction Layer through Band Alignment. *J. Mater. Chem. A* **2018**, *6*, 16920-16931.

60. Heo, J. H.; You, M. S.; Chang, M. H.; Yin, W.; Ahn, T. K.; Lee, S.-J.; Sung, S.-J.; Kim, D. H.; Im, S. H. Hysteresis-Less Mesoscopic Ch 3 Nh 3 Pbi 3 Perovskite Hybrid Solar Cells by Introduction of Li-Treated Tio 2 Electrode. *Nano Energy* **2015**, *15*, 530-539.

61. Mott, N. F. N. F., Sir; Gurney, R. W. R. W. *Electronic Processes in Ionic Crystals*, 2nd ed ed.; Clarendon Press, 1948.

TOC Graphic

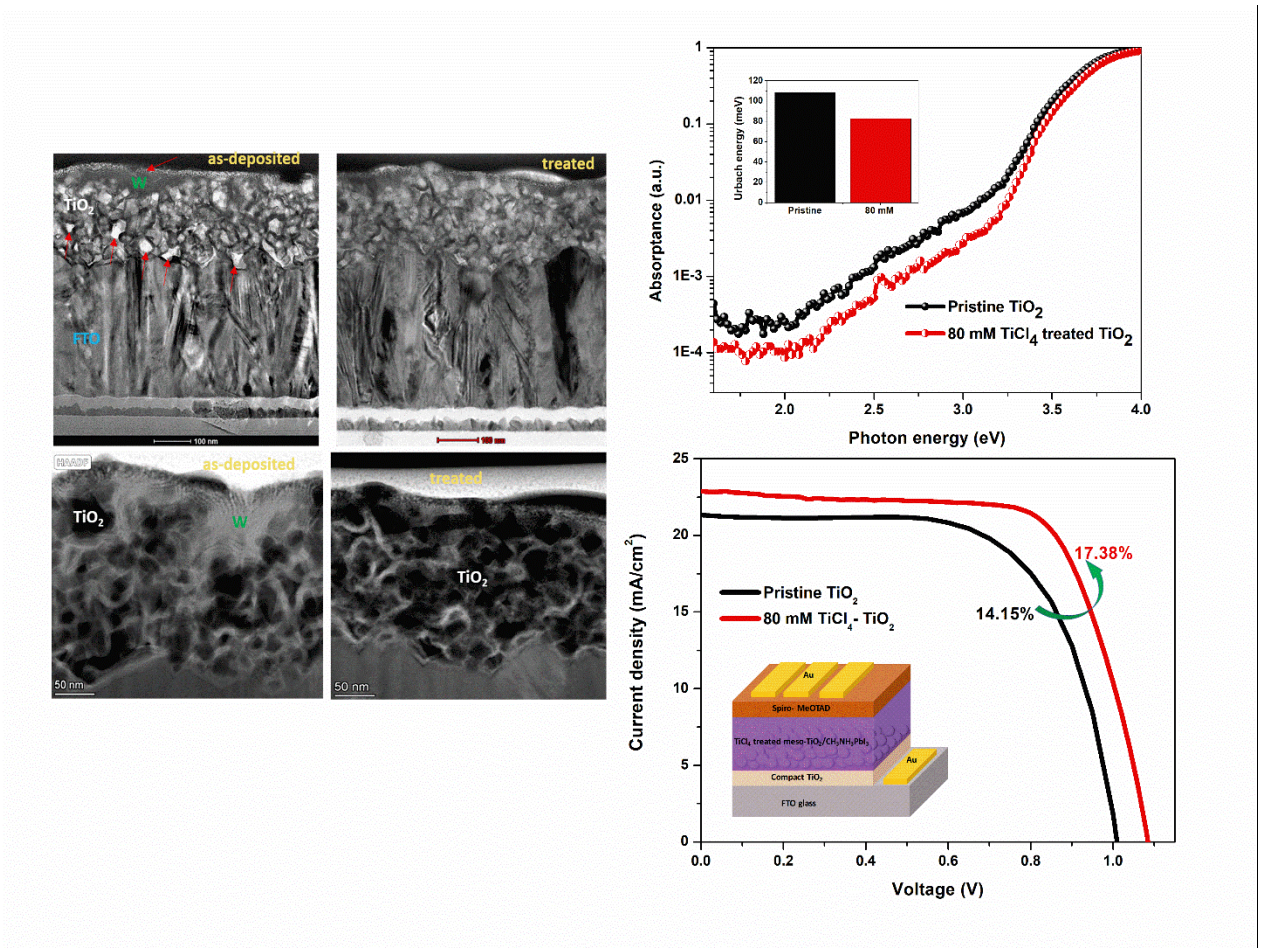
as-deposited
treated
TiO2
W
FTD
100 nm
HAADF
as-deposited
treated
TiO2
W
TiO2
50 nm
50 nm
Absorptance (a.u.)
Photon energy (eV)
Urbach energy (meV)
Pristine
80 mM
Pristine TiO2
80 mM TiCl4 treated TiO2
Current density (mA/cm2)
Voltage (V)
17.38%
14.15%
Pristine TiO2
80 mM TiCl4- TiO2
Au
Spiro- MeOTAD
TiCl4 treated meso-TiO2/CH3NH3PbI3
Compact TiO2
FTO glass
Au